Supplementary Figures and Discussion for: Entrained debris records regrowth of the Greenland Ice Sheet after the last interglacial

Nicholas Holschuh[1*], Christianson Knut[2], Dienstfrey William[2], Hills Benjamin[3], Hoffman Andrew[4], Paden John[5], Winter Kate[6], Zuraw Ruth[1]

[1*]Department of Geology, Amherst College, P.O. Box 5000, Amherst, MA, 01002-5000, MA, USA.
[2]Department of Earth and Space Sciences, University of Washington.
[3]Department of Geophysics, Colorado School of Mines.
[4]Marine and Polar Geophysics, Lamont-Doherty Earth Observatory.
[5]Center for Remote Sensing and Integrated Systems (CReSIS), University of Kansas.
[6]School of Geography and Natural Sciences, Northumbria University, UK, Northumbria University.

*Corresponding author(s). E-mail(s): nholschuh@amherst.edu;
Contributing authors: knut@uw.edu; w.dienstfrey@gmail.com; benjamin.hills@mines.edu; aoh2111@columbia.edu; paden@ku.edu; k.winter@northumbria.ac.uk; rzuraw25@amherst.edu;

Keywords: Greenland, MIS 5e, Englacial Debris, Ice Penetrating Radar

Extended Data Figures

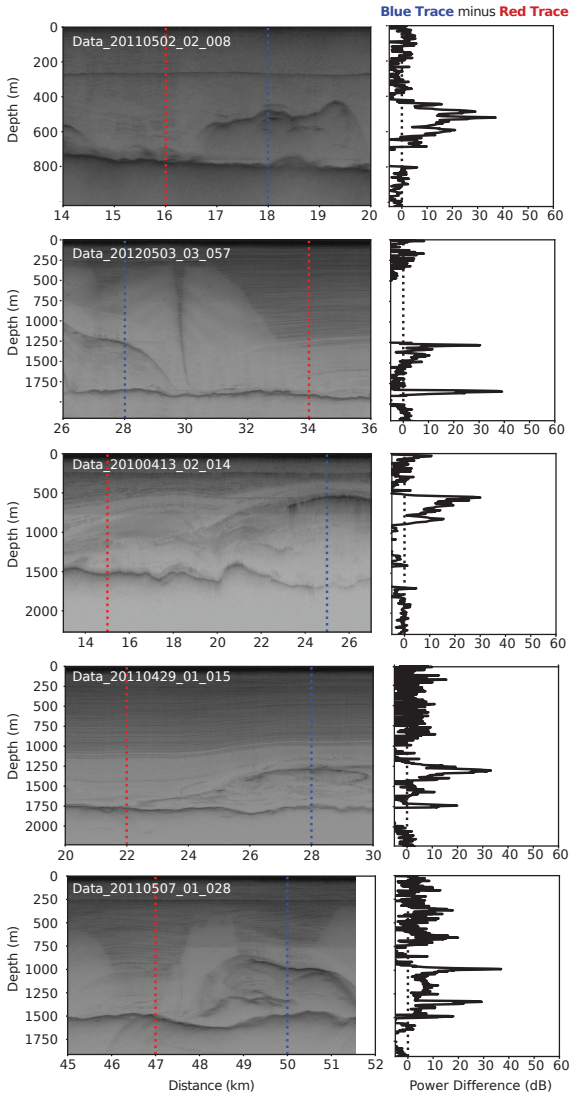

Fig. 1 Collection of radargrams from Northern Greenland with highlighted traces containing debris trains (blue) and meteoric layering (red). The power difference between those traces (blue minus red) is presented in the column on the right.

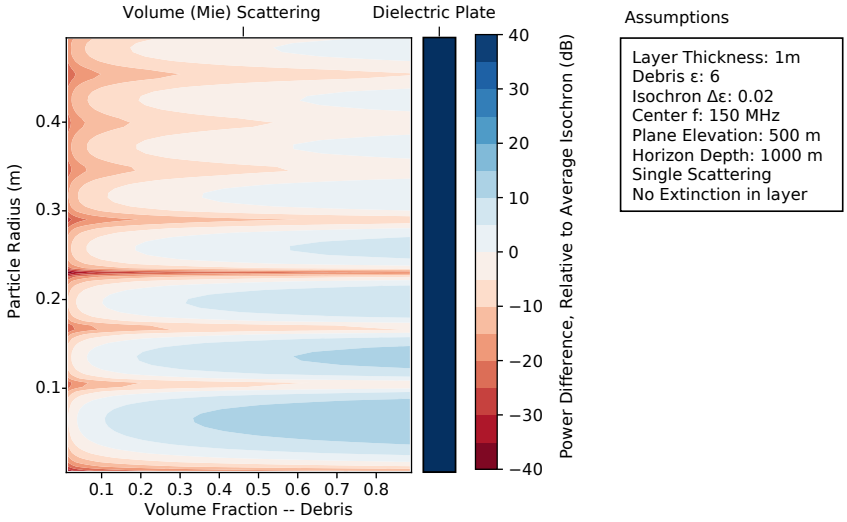

Fig. 2 A plot of expected reflection power for debris trains comprised of spherical particles (left) and for a dielectric plate of the same debris material (right), relative to typical isochronous layering.

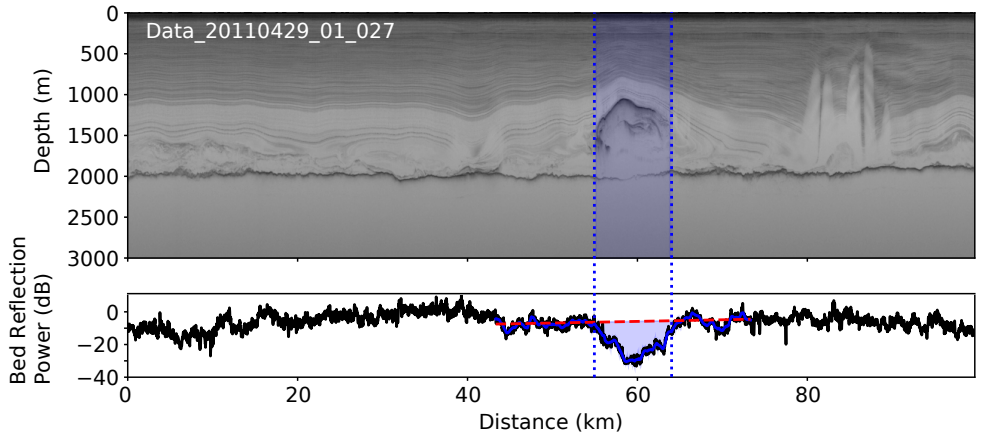

Fig. 3 A radar image from Northern Greenland with co-located bed reflection power, showing apparent power losses below only the debris rich portion of the englacial structure.

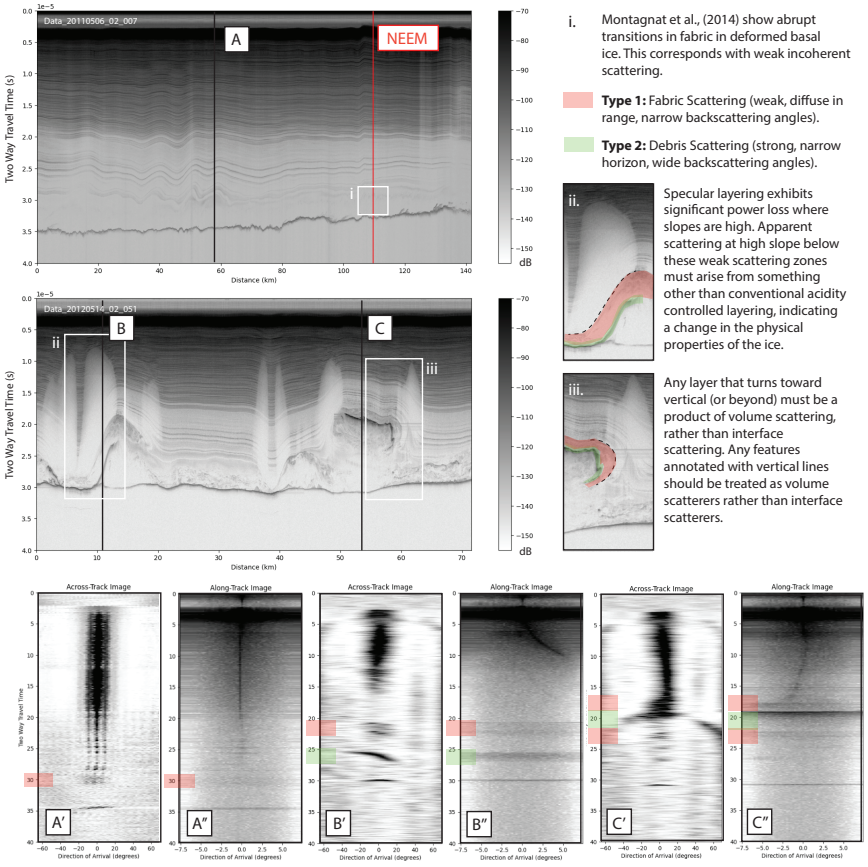

Fig. 4 Radar imagery capturing the different scattering behavior described in this manuscript, with information from three individual traces (A, B, C) highlighting categorical differences in scattering phenomena. The top panel includes a radar image spanning the NEEM ice core, where direct measurements of subsurface material properties show that incoherent scattering is generated at fabric transitions. The middle panel emphasizes a qualitative change in the nature of scattering with depth, where specular meteoric layers are lost where they dip steeply, but incoherent scattering persists at depth, enabling imaging of very steeply bounded structures.

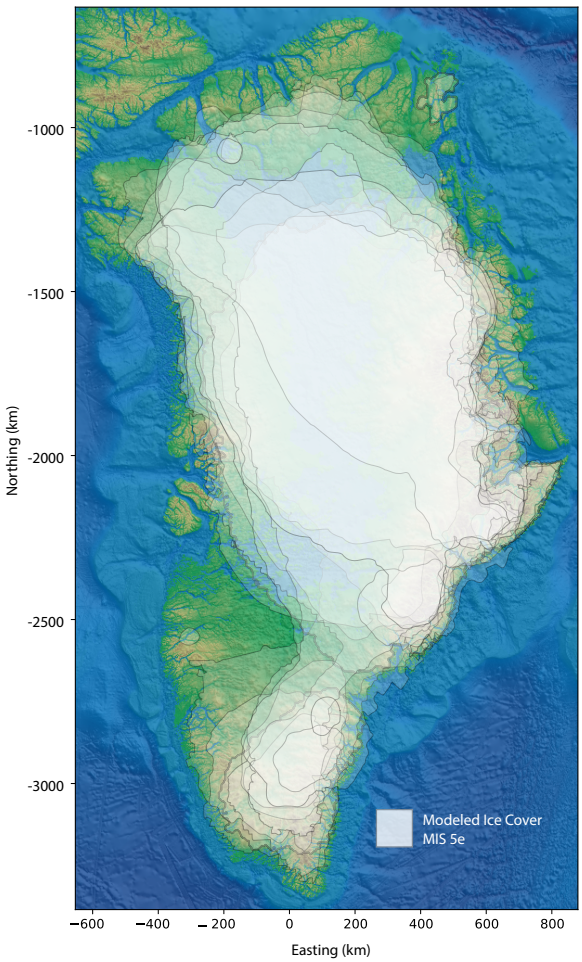

Fig. 5 Map showing modeled ice coverage during MIS 5e [1–7].

We have also assembled a set of animations that aided us in radar interpretation, highlighting the relationships between along- and across-track scattering directions, as well as power variation in the ice bottom reflector.

- Extended Data Figure 6: Example Along and Across Track Direction of Arrival Animation
- Extended Data Figure 7: Nadir to off-nadir profile comparison
- Extended Data Figure 8: Along and Across Track Direction of Arrival Animations
- Extended Data Figure Collection: Scattering Direction and Amplitude Information for All Measured Debris Trains

1 Supplementary Discussion 1: Interpreting conventional and swath radar data jointly

In this paper, we infer three different types of scattering, differentiated by backscattering amplitude and direction of arrival information. The scattering types we identified are: specular scattering from meteoric layering, weak incoherent scattering from a narrow angular range (type 1), and strong incoherent scattering measured across a wide angular range (type 2).

Measured backscattering amplitude is a product of both scatterer properties and path effects. For debris trains, we attempt to isolate scatterer properties by comparing their signal character to targets at similar depth within the ice sheet, assuming path effects (ohmic and scattering losses) do not vary substantially in the shallow ice (an assumption we re-evaluate for deeper targets). From amplitude alone, debris trains are distinct, with reflection powers up to 30 dB higher than meteoric layering at comparable depths (Extended Data Fig. 1).

This difference must be explained by dielectric or geometric differences in the nature of the scattering targets. Here, we calculate the non-dimensional backscattering cross-sections for specular meteoric layering and for volumetric scattering from debris rich layers to evaluate whether or not 30 dB can be explained by entrained debris. We start with the following simplified form of the radar equation:

$$P^r = \frac{S}{4\pi(z_{air}+z_{ice})^2} \; A\sigma_0 \; \frac{1}{4\pi(z_{air}+z_{ice})^2} \; e^{-2\alpha z_{ice}} \tag{1}$$

Because the source properties described by S (transmit power, antenna gain, receiver aperture size) do not change along a radar profile and we are comparing targets at equal range ($z_{air} + z_{ice}$) and depth (z_{ice}), observed power variability must arise from changes in the radar cross section ($A\sigma_0$) or the attenuation rate (α). If we assume that attenuation rates in the top half of the ice column are small and relatively homogeneous (typical for cold ice), the extra backscattered energy from debris trains (30+ dB) must be explained by differences in the radar cross section of the targets. For specular, dielectric planes with power reflection coefficient, R, the radar cross section is defined as:

$$A\sigma_0 = R\frac{4\pi}{\lambda^2}A^2 \tag{2}$$

For most radar systems, the illumination area (A) is not beam limited, instead defined by the first Fresnel zone of the system:

$$A = \frac{\pi\lambda}{4}\left(z_{air} + \frac{z_{ice}}{\sqrt{\epsilon_i}}\right) \tag{3}$$

This produces a total radar cross section with the following form:

$$A\sigma_0 = R\pi^3\left(z_{air} + \frac{z_{ice}}{\sqrt{\epsilon_i}}\right)^2 \tag{4}$$

Mie scattering theory gives us a framework for calculating the non-dimensional radar-cross section for volumetric scattering layers [8]. Here, we use "miepython" [9]

to calculate the back scattering efficiencies (Q_{back}) for debris of different sizes (defined by particle radius r). This can then be used to find the integrated radar cross section using an assumed particle number-density (N, generated from an assumed volume fraction, p). Defining the illuminated area to the first fresnel zone and assuming some layer thickness (z_l), we can produce the total radar cross section for Mie scattering from debris:

$$N = \frac{3p}{4\pi r^3} \tag{5}$$

$$A\sigma_0 = \underbrace{\pi r^2 Q_{back}}_{\text{particle backscattering}} \underbrace{NAz_l}_{\text{number of particles}}$$

$$A\sigma_0 = \pi r^2 Q_{back} N \frac{\pi \lambda z_l}{4} \left(z_{air} + \frac{z_{ice}}{\sqrt{\epsilon_i}} \right) \tag{7}$$

In extended data figure 2, we present the expected backscattered energy from a debris rich layer as a function of debris particle radius and debris volume fraction (assuming a dielectric permittivity of debris equal to 6). Values represent the power anomaly, relative to scattering from isochrons (defined by a dielectric permittivity that is 0.02 higher than background) at comparable depths. In addition to scattering from a debris rich layer comprised of spherical particles, we calculate the expected scattering anomaly associated with a dielectric plate consisting entirely of debris material (which can be thought of as the high end-member value for scattering from subglacial material entrained in ice).

For the debris rich layer, smaller particle size and high concentrations promote elevated backscattering, with the highest values found for debris at the centimeter scale. But no combination of debris size and concentration can reproduce the 30 dB signal we observe in the radar data. This is likely due to a limitation in our approach: our radar cross section does not include contributions from multiple scattering, which will increase the total backscattered energy. The observed value does fall below the dielectric plate end-member, indicating the measured signal is consistent with mixture of ice and rock. Future radiative transfer modeling capable of capturing multiple scattering from the debris rich layer would present a major advance in our understanding of complex scattering sources in ice sheets.

This analysis raises the question: could all diffuse scattering arise from debris, even the weak (and narrow angle) type 1 scattering we identified. Previous studies show that fabric is capable of generating incoherent scattering as well. Weak incoherent scattering was identified in Northern Greenland, corresponding with abrupt changes in fabric in the NEEM ice core ([10], and Extended Data Fig. 5.i). There also appear to be deep isochrons in the deep ice that scatter at a range of angles (and can be seen even in steeply dipping areas), where we know subglacial debris is unlikely. For those layers, we believe deposition impurities localize fabric development, and drive fabric transitions that explain the cone of scattering at amplitudes comparable to other isochronous layering. This phenomenon is also seen immediately above debris trains, where we expect strain may be localized (Extended Data Fig. 5.ii/iii).

In addition to the nature of the scattering from within the structures, another indication for debris is the reduced backscattering by the ice sheet bed below debris trains in many places. Extended data figure 3 provides one example of normalized bed echo power from beneath an observed structure. Three interpretations of the apparent diminution of reflection power are possible: (1) that there is a significant change in the character of the bed itself that leads to lower reflectivity, (2) that the ice within the structure is warm or rich in proton defects that drive ohmic losses [11], or (3) that significant dielectric contrasts within the ice drive scattering losses along the path [12]. For typical substrate materials, that observed power change would require a uniformly wet bed in all places surrounding these structures and frozen till or bedrock only underneath them [13], which is inconsistent with the expected modern thermal structure of the ice sheet. In addition, power losses are more local to areas with high englacial scattering rather than extended beneath the full volume of deformed basal ice. Power losses also show no clear intensification with basal ice thickness (expected for ohmic losses). Thus, we argue this phenomenon arises from extinction by Mie scattering off englacial debris, and the data do not show elevated ice temperature within these structures.

2 The effect of fluidity errors on model performance

Ice flow is accommodated by two mechanisms: sliding and deformation. As implemented in ice sheet models, both processes are commonly represented by a power law, describing how a given stress (τ) is translated into motion observed at the surface (u_o) given a power-law exponent (m or n) and a prefactor, the basal sliding coefficient (C) or the ice fluidity (A).

$$u_o = \left(\frac{\tau}{C}\right)^m + \int_0^h A\tau^n \, dz \tag{8}$$

Although the precise values of m and n are still debated, we assume those are fixed, then, model initialization requires assigning values for A and C that reproduce observed surface velocities. But with a single constraint, they cannot be uniquely determined. As a result, A is often assumed and C is solved for by inversion, minimizing errors between modeled and observed surface velocities. Errors in the assumed value of A will produce errors in the inversion for C, and together will then change the responsiveness of model ice sheets to future changes in stress. Here, we investigate how systematic errors in A might affect model projections.

Consider the case where an initialized model underestimates the fluidity of deep ice. To correct the model such that it reflects the reality of the system, one would need to increase fluidity from A to $A + \Delta A_e$. In this case, the original model must also have been underestimating the value of C. Thus, with the addition of ΔA_e there must also be an addition of ΔC_e in order to reproduce the same initial velocity:

$$\left(\frac{\tau}{C}\right)^m + \int_0^h A\tau^n \, dz = \left(\frac{1}{[C + \Delta C_e]}\tau\right)^m + \int_0^h [A + \Delta A_e]\tau^n \, dz \tag{9}$$

If we assume a depth-independent value for A (i.e., $\bar{A}$), we can reframe equation 9 in terms of a new set of constants, $\gamma_c = C^{-m}$ and $\gamma_a = \bar{A}$, such that:

$$u_o = \gamma_c \tau^m + \gamma_a \frac{\tau^{n+1}}{n+1} = (\gamma_c + \Delta\gamma_c)\tau^m + (\gamma_a + \Delta\gamma_a)\frac{\tau^{n+1}}{n+1} \tag{10}$$

$$-\Delta\gamma_c \tau^m = \frac{\Delta\gamma_a \tau^{n+1}}{n+1} \tag{11}$$

$$\Delta\gamma_c = -\frac{\Delta\gamma_a \tau^{n+1-m}}{n+1} \tag{12}$$

With this definition, we can explore how these error terms (ΔA_e and ΔC_e, or alternatively, $\Delta\gamma_a$ and $\Delta\gamma c$) modify the velocity response to changes in stress.

Consider applying a small stress perturbation $\delta\tau$ to a system with constant C and A. We can then obtain the following relationships for sliding-accommodated flow, deformation, and both together:

$$u_s + \delta u_s = \left(\frac{\tau + \delta\tau}{C}\right)^m \tag{13}$$

$$u_d + \delta u_d = \int_0^h A(\tau + \delta\tau)^n \, dz \tag{14}$$

$$\begin{aligned} u_o + \delta u_o &= u_s + \delta u_s + u_d + \delta u_d \\ &= \left(\frac{\tau + \delta\tau}{C}\right)^m + \int_0^h A(\tau + \delta\tau)^n \, dz \end{aligned} \tag{15}$$

In the limit that $\tau >> \delta\tau$, we can pull out a factor of τ^m and τ^n from the sliding and deformation velocity components, respectively and use the binomial approximation to simplify the expressions. Dropping higher order terms in $\delta\tau$ we obtain the following form relating δu_o and $\delta\tau$.

$$\begin{aligned} \delta u_o &= \left(\frac{\tau + \delta\tau}{C}\right)^m + \int_0^h A(\tau + \delta\tau)^n \, dz - u_o \\ &= \left(\frac{\tau}{C}\right)^m \left(1 + \frac{m\delta\tau}{\tau}\right) - \left(\frac{\tau}{C}\right)^m + \int_0^h A\tau^n \left(1 + \frac{\delta\tau}{\tau}\right)^n dz - \int_0^h A\tau^n \, dz \\ &= \left[\frac{m\tau^{m-1}}{C^m} + \int_0^h A\tau^{(n-1)} \, dz\right] \delta\tau \end{aligned} \tag{16}$$

Therefore:

$$\frac{\delta u_o}{\delta\tau} = \frac{m\tau^{m-1}}{C^m} + \int_0^h A\tau^{n-1} \, dz \tag{17}$$

Following the same simplification used in equation 10, we can reduce the stress derivative to the following:

$$\frac{\delta u_o}{\delta\tau} = m\gamma_c \tau^{m-1} + \gamma_a \tau^n \tag{18}$$

We refer to the left-hand side of this equation ($\frac{\delta u_o}{\delta \tau}$) as the "stress-response" of a given model; that is, how stress evolution will lead to speed change. We can use this function to explore how errors in fluidity result in errors in the stress-response of the system:

$$\begin{aligned}
\frac{\delta u_o}{\delta \tau}_{\text{error}} &= \frac{\delta u_o}{\delta \tau}_{\text{reality}} - \frac{\delta u_o}{\delta \tau}_{\text{model}} \\
\frac{\delta u_o}{\delta \tau}_{\text{error}} &= m(\gamma_c + \Delta\gamma_c)\tau^{m-1} + (\gamma_a + \Delta\gamma_a)\tau^n - (m\gamma_c\tau^{m-1} + \gamma_a\tau^n) \\
&= m\Delta\gamma_c\tau^{m-1} + \Delta\gamma_a\tau^n \\
&= \frac{-m}{n+1}(\Delta\gamma_a\tau^{n+1-m})\tau^{m-1} + \Delta\gamma_a\tau^n \\
&= \frac{n+1-m}{n+1}\Delta\gamma_a\tau^n
\end{aligned} \tag{19}$$

This reveals an important phenomenon: the effect of errors in viscosity will depend on the exponent used for the viscous flow and sliding power laws, with a qualitative change in system dynamics at n = m+1 (with typically values for n being 3-4). To better understand why this behavior emerges, we can consider four scenarios:

- True ice fluidity is less than the model assumed fluidity, and the model uses a linear viscous sliding law (ΔA and $\Delta\gamma_a$ are < 0, $m < n+1$): the model will be more responsive to stress changes than the true system ($\frac{\delta u_o}{\delta \tau}_{\text{error}} < 0$).
- True ice fluidity is less than the model assumed fluidity, and the model uses a nearly-plastic sliding law (ΔA and $\Delta\gamma_a$ are < 0, $m > n+1$): the model will be less responsive to stress changes than the true system ($\frac{\delta u_o}{\delta \tau}_{\text{error}} > 0$).
- True ice fluidity is greater than the model assumed fluidity, and the model uses a linear viscous sliding law (ΔA and $\Delta\gamma_a$ are > 0, $m < n+1$): the model will be less responsive to stress changes than the true system ($\frac{\delta u_o}{\delta \tau}_{\text{error}} > 0$).
- True ice fluidity is greater than the model assumed fluidity, and the model uses a nearly-plastic sliding law (ΔA and $\Delta\gamma_a$ are > 0, $m > n+1$): the model will be more responsive to stress changes than the true system ($\frac{\delta u_o}{\delta \tau}_{\text{error}} < 0$).

The net effect ultimately depends on the nature of the model error (was the ice too strong and the bed too weak, or the ice too weak and the bed too strong) and which physical law is more responsive to changes in stress. If the model error is such that the ice is too weak and ice deformation is more responsive to stress changes than sliding is, then the model will be more responsive to stress changes than the real ice sheet. If the model error is such that the ice is too strong and ice deformation is more responsive to stress changes than sliding, than the model will be less responsive to stress changes than the real ice sheet. This leads to a somewhat counterintuitive results in circumstances with a nearly-plastic sliding law: models that do not include high fluidity anomalies in the deep ice, which we infer in this study, will be more responsive to stress changes than the true ice sheet.

References

[1] Born, A. & Nisancioglu, K. H. Melting of Northern Greenland during the last interglaciation. *The Cryosphere* **6**, 1239–1250 (2012). URL https://tc.copernicus.org/articles/6/1239/2012/.

[2] Robinson, A., Calov, R. & Ganopolski, A. Greenland ice sheet model parameters constrained using simulations of the Eemian Interglacial. *Climate of the Past* **7**, 381–396 (2011). URL https://cp.copernicus.org/articles/7/381/2011/.

[3] Christ, A. J. *et al.* Deglaciation of northwestern Greenland during Marine Isotope Stage 11. *Science* **381**, 330–335 (2023). URL https://www.science.org/doi/10.1126/science.ade4248.

[4] Helsen, M. M., Van De Berg, W. J., Van De Wal, R. S. W., Van Den Broeke, M. R. & Oerlemans, J. Coupled regional climate–ice-sheet simulation shows limited Greenland ice loss during the Eemian. *Climate of the Past* **9**, 1773–1788 (2013). URL https://cp.copernicus.org/articles/9/1773/2013/.

[5] Tarasov, L. & Peltier, W. R. Greenland glacial history, borehole constraints, and Eemian extent: GREENLAND GLACIAL HISTORY. *Journal of Geophysical Research: Solid Earth* **108** (2003). URL http://doi.wiley.com/10.1029/2001JB001731.

[6] Schaefer, J. M. *et al.* Greenland was nearly ice-free for extended periods during the Pleistocene. *Nature* **540**, 252–255 (2016). URL https://www.nature.com/articles/nature20146.

[7] Otto-Bliesner, B. L. *et al.* Simulating Arctic Climate Warmth and Icefield Retreat in the Last Interglaciation. *Science* **311**, 1751–1753 (2006). URL https://www.science.org/doi/10.1126/science.1120808.

[8] Ulaby, F. T. & Long, D. G. *Microwave Radar and Radiometric Remote Sensing* (University of Michigan Press, 2015).

[9] Prahl, S. miepython: A Python library for Mie scattering calculations (2025). URL https://github.com/scottprahl/miepython.

[10] Mutter, E. L. & Holschuh, N. Advancing interpretation of incoherent scattering in ice penetrating radar data used for ice core site selection. *The Cryosphere* **19**, 3159–3176 (2025). URL https://egusphere.copernicus.org/preprints/2024/egusphere-2024-2450/.

[11] MacGregor, J. *et al.* Radar attenuation and temperature within the Greenland Ice Sheet. *Journal of Geophysical Research: Earth Surface* 983–1008 (2015).

[12] Winter, K. *et al.* Radar-Detected Englacial Debris in the West Antarctic Ice Sheet. *Geophysical Research Letters* **46**, 10454–10462 (2019). URL https://onlinelibrary.wiley.com/doi/abs/10.1029/2019GL084012.

[13] Peters, M. E., Blankenship, D. D. & Morse, D. L. Analysis techniques for coherent airborne radar sounding: Application to West Antarctic ice streams. *Journal of Geophysical Research: Solid Earth* **110**, 2004JB003222 (2005). URL https://agupubs.onlinelibrary.wiley.com/doi/10.1029/2004JB003222.